### A Numerical and Experimental Study of the Bistable-Unstable Transition in Pressurized Flexible Disk Files

The bistable operating region of flexible disk files is limited at decreasing air flow rates by a transition at which undesirable gaps appear in the otherwise uniformly spaced disks of the pack. These spontaneous gaps, as opposed to the externally controlled gaps of the bistable range, are a consequence of local air flow fields at the outer edge of the disks. Experiments with external shrouds of various clearance showed axial periodicity in the occurrence of the gaps and provided physical insight which led to quantitative numerical solution of the nonlinear fluid equations. Two scales of the flow, i.e., the flow between individual disks and a peripheral unstable Couette flow, are found to couple in such a manner as to delineate the transition.

#### Introduction

A flexible disk pack arrangement is illustrated in Fig. 1(a) together with associated parameter definitions. The disks are separated at the spindle by permeable mesh spacers and the pack has rigid base plates mounted on each end [1]. The entire assembly rotates about its axis with angular velocity  $\Omega$  and air is pumped through the pack at a flow rate O per disk. Figure 1(b) depicts three regimes of different pack behavior first observed by McGinnis, Orlando, and Weidenhammer [1]. In the high-Q, or stable, regime the pack closes itself after it is opened by external means. In the mid-Q, or bistable, regime the closed pack configuration is stable, but an opening in the pack caused by external means is also stable. In the low-Q, or unstable, regime the closed pack configuration is not stable and the pack breaks up into subpacks with reduced disk spacing and open gaps. The critical flow rate Q\* that defines the transition from the bistable to the unstable regime, and the gap-subpack structure, depend on several physical parameters of the pack. Experimental designs for possible use in magnetic recording have employed external means to produce gaps while operating in the bistable range to permit accessing of individual disks with a recording head. From a design viewpoint, the bistable regime is best defined by its lower boundary, i.e., the bistable-unstable transition line  $Q^*$  vs.  $\Omega$ . The object

of this study is to identify the underlying physical mechanism that causes the transition and to quantitatively describe the transition in terms of pack design parameters.

On the basis of experimental investigations, we conjecture that the formation of gaps at the transition is due to an invasion of toroidal vortices into the spacing be-

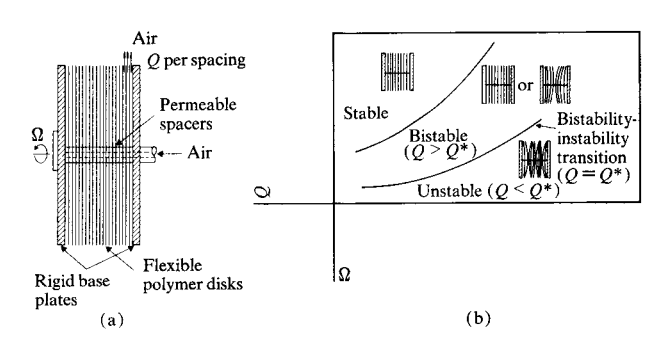


Figure 1 (a) Disk pack parameters;  $r_i$  = inside radius;  $r_0$  = outside radius; d = disk thickness; s = hub spacing;  $\Omega$  = rotation speed;  $Q^*$  = critical flow rate/disk;  $\nu = \mu/\rho$  = kinematic viscosity of air;  $R = s^2\Omega/\nu$ ;  $\varepsilon^* = Q^*/2\pi r_0 s^2\Omega$ . (b) Stable, bistable, and unstable regimes of Q- $\Omega$  plane.

Copyright 1979 by International Business Machines Corporation. Copying is permitted without payment of royalty provided that (1) each reproduction is done without alteration and (2) the *Journal* reference and IBM copyright notice are included on the first page. The title and abstract may be used without further permission in computer-based and other information-service systems. Permission to *republish* other excerpts should be obtained from the Editor.

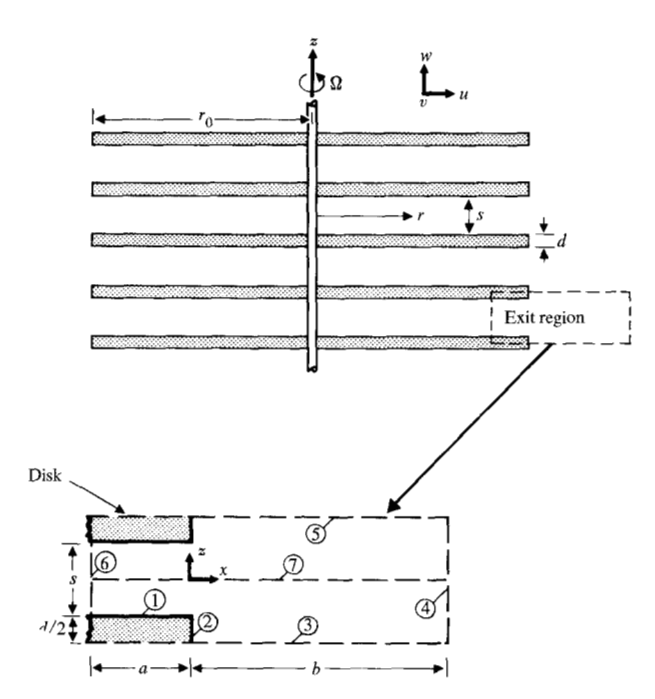


Figure 2 Sketch of disk pack exit region of computation.

tween disks at the disk edges. Uniform disk spacing is restored by blowing out or otherwise annihilating these vortices. It is apparent that a theoretical description of such a recirculating flow cannot be made on the basis of boundary layer equations, but requires instead the elliptic system of Navier-Stokes equations. The numerical solution of this problem has been previously obtained by the authors [2]. Due to the large swirl Reynolds number,  $r_0^2 \Omega / \nu \simeq 2.5 \times 10^5$  (for disks of radius  $r_0$  rotating with angular velocity  $\Omega$  in air with viscosity  $\nu$ ), we restricted our analysis in [2] to a small exit region which is relatively far from the rotation center (Fig. 2). Using an approximation scheme, we derived equations with an effective Reynolds number which was smaller than the one above by a factor of  $\sim 10^4$  to  $10^6$ . Computations were carried out in [2] for several values of flow rate and Reynolds number. These results depend, of course, on the boundary conditions assumed for the small exit region. Considerable experimental and computational effort was therefore aimed at determining the correct downstream conditions at operational rotation rates.

In the second section of this paper, we give a brief outline of the computation scheme employed in [2]. Then, in the third section, we describe briefly the experiments that were conducted in order to understand the flow field outside the disk pack. This information was necessary to supply the appropriate downstream boundary conditions. We concluded from these experiments that, when the shroud is present, the flow between the disk pack and

shroud has toroidal ring cells, as first observed experimentally and described theoretically for flow between coaxial rotating cylinders by Taylor [3]. These Taylor cells occur as a result of an instability in circular Couette flow. If the outer cylinder is fixed, circular flow is stable provided that the inner cylinder rotates slowly enough and/or the spacing between the cylinders is small enough. Our experiments led us to conclude that the downstream boundary condition is determined in the case of a shrouded pack by the Taylor cells. The exact downstream flow for the shrouded pack can be determined quantitatively by numerical computation. As the shroud clearance is increased, results appropriate to the unshrouded pack are obtained.

In the fourth section, we use the numerical scheme of [2], with appropriate modification, to calculate the flow between a rotating disk pack and a fixed shroud, and thereby we determine the downstream conditions for flow in the pack. For this purpose we modeled the disk pack as a rotating cylinder and obtained solutions for various shroud clearances. The solutions obtained in this manner exhibit the expected Taylor cells. These flow fields are periodic in the axial direction, with a wavelength essentially the same as the thickness of the subpacks. For small clearance shrouds, we are near neutral stability for circular Couette flow and the Taylor cells are steady. This result was determined numerically and is found to be in agreement with an extensive experimental study of Coles [4]. When the spacing is increased, corresponding to increased Taylor number, Coles shows that the Taylor cells do not remain axisymmetric but become periodic in the azimuthal direction, and the azimuthal harmonic waves propagate in this direction with a speed considerably less than that of the cylinder. At even wider spacing the flow becomes turbulent. For these reasons, increasing difficulty was encountered in computing flows for shrouds with wider clearance. This means that we may not be able to calculate directly the downstream boundary conditions for the case of no shroud. Since the pack behavior is qualitatively the same for the shrouded and unshrouded packs, and since the Taylor cells appear to supply the correct boundary conditions for the shrouded case, we expect that some axially periodic but time-varying structure is present in the flow close to the disk edges even in the absence of a shroud.

After this, in the fifth section, we use these calculated downstream conditions to obtain, as in Ref. [2], numerical solutions corresponding to the exit region flow (Fig. 2) between the disks. Then, in the sixth section, before conclusions are presented in the final section, we compare numerically predicted behavior with the experimentally determined bistability.

#### Numerical solution for exit region flow—free downstream condition

Consider the disk pack configuration shown in Fig. 2. For the purposes of the flow calculation we assume that the disks are rigid and evenly spaced and that they rotate with angular velocity  $\Omega$ . We confine our attention to the small exit region far from the center of rotation and assume axial periodicity. We start with the axisymmetric Navier-Stokes equations for a viscous incompressible fluid. If u, v, and w represent the cylindrical polar components of fluid velocity relative to the rotating disk, we assume, in the small exit region of Fig. 2,

$$\frac{u}{s\Omega} = u_1 + \delta u_2 + \cdots,$$

$$\frac{v}{s\Omega} = v_1 + \delta v_2 + \cdots,$$

$$\frac{w}{s\Omega} = w_1 + \delta w_2 + \cdots, \tag{1}$$

where s is the spacing between adjacent disks and

$$\delta = s/r_0 << 1. (2)$$

Changing to local coordinates by

$$r = r_0 + x = (s + \delta x)/\delta, \tag{3}$$

we obtained in [2] the equations

$$v_{1_t} + (u_1 v_1)_x + (w_1 v_1)_z = R^{-1} (v_{1_{xx}} + v_{1_{zz}}) - 2u_1,$$

$$\omega_{1_t} + (u_1 \omega_1)_x + (w_1 \omega_1)_z = R^{-1} (\omega_{1_{xx}} + \omega_{1_{zz}}) - 2v_{1_z},$$

$$u_{1_x} + w_{1_x} = 0, \qquad \omega_1 = w_{1_x} - u_{1_z}.$$
(4)

Here, subscripted letters denote partial differentiation with respect to dimensionless time  $t(t=t'\Omega)$  and coordinates x, z(x=x'/s, z=z'/s), primes being used for physical quantities) and the effective Reynolds number R is defined by

$$R = s^2 \Omega / \nu. ag{5}$$

We introduce the stream function  $\psi$  through

$$u_1 = \psi_r, \ w_1 = -\psi_r, \tag{6}$$

so that the third equation of (4) is identically satisfied and the last equation of (4) becomes

$$\omega_1 = -(\psi_{xx} + \psi_{zz}). \tag{7}$$

By use of (6), we can eliminate  $u_1$ ,  $w_1$  in the first and second equations of (4) and thereby obtain with (7) three equations in  $v_1$ ,  $\omega_1$  and  $\psi$ .

In order to solve the above equations in the small exit region in Fig. 2, we employ finite difference methods. This requires boundary conditions on the lines 1-4, 6 and 7. We must also choose the values a, b which determine

the radial extent of the region in question. The value of R corresponding to typical pack parameters of Fig. 1(a) is R = 0.133, and on the basis of previous studies we expect the values at x = -a/s to agree with the boundary layer solution, i.e.,

$$u_{1} = -6\varepsilon(z^{2} - 1/4),$$

$$v_{1} = -\varepsilon R(z^{2} - 5/4)(z^{2} - 1/4),$$

$$w_{1} = 0, \ \psi = -\varepsilon(4z^{3} - 3z - 1)/2, \quad \omega_{1} = 12\varepsilon z$$

$$\begin{cases}
at \ \textcircled{6}, \\
\end{cases}$$
(8)

where

$$\varepsilon = Q/2\pi r_{\rm o} s^2 \Omega. \tag{9}$$

For the closely spaced pack rotating in an unbounded fluid, we expect the values at x = b/s to correspond (under certain conditions) to the steady circular flow field, which appears in our variables as

$$u_1 = \varepsilon (1 + d/s)^{-1}, \quad v_1 = 2x, \quad w_1 = 0$$

$$\psi_1 = u_1 z, \quad \omega_1 = 0$$
at 4. (10)

Rather than force-match our solution to the values given by (8), (10) at lines 6, 4, we used instead the "slow change" free conditions

$$\psi_{xx} = \omega_{1_{xx}} = v_{1_{xx}} = 0 \text{ at } \textcircled{6}, \textcircled{4}$$
 (11)

and allowed the entrance and exit profiles to develop. We could then compare the results with the expected profiles (8), (10) and thereby obtain some indication that the radial extent of our exit region was chosen sufficiently large. On lines 1, 2 in Fig. 2, we used "no-slip" conditions and on lines 3, 7 we used symmetry, with  $\psi=0$  at line 3 and  $\psi=\varepsilon/2$  at line 7, to match the source strength. Readers interested in the details of the calculation procedure are referred to [2].

The value of the dimensionless flow rate parameter  $\varepsilon$ , corresponding to typical operating conditions, is  $\varepsilon=0.7$ . Figure 3 shows the results of the numerical computations for R=0.133 and  $\varepsilon=0.7$  (with a=s, b=7s/3) using four graphs. In the upper right graph, the exit region stream lines (dashed) and vorticity lines (solid) are given. The interval values are indicated in Table 1, and the algebraic sign is positive for dashed lines when the dashes have equal length (negative for unequal length). The sign is positive for solid lines when they are smooth (negative when ticked). In the lower right graph are shown lines of constant azimuthal velocity (dashed) and, again, vorticity (solid). In the upper left graph, radial velocity profiles at the inlet x=-1 (solid) and at the disk edge x=0 (dashed) are shown; and in the lower left graph, azimuthal velocity

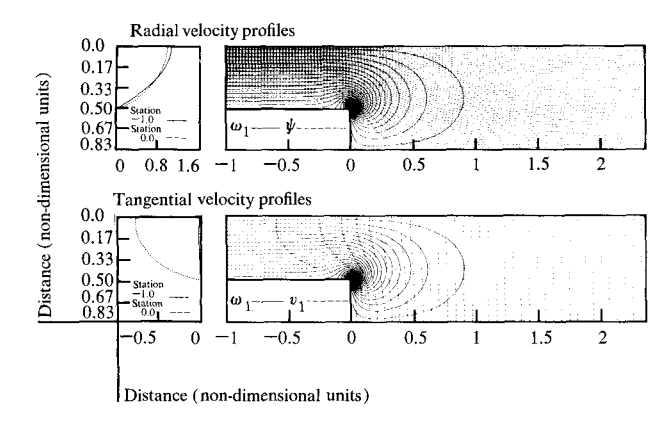


Figure 3 Exit region flow for R=0.133,  $\varepsilon=0.7$  at t=0.085 with free downstream condition;  $v_{1_x}=-2.0$ .

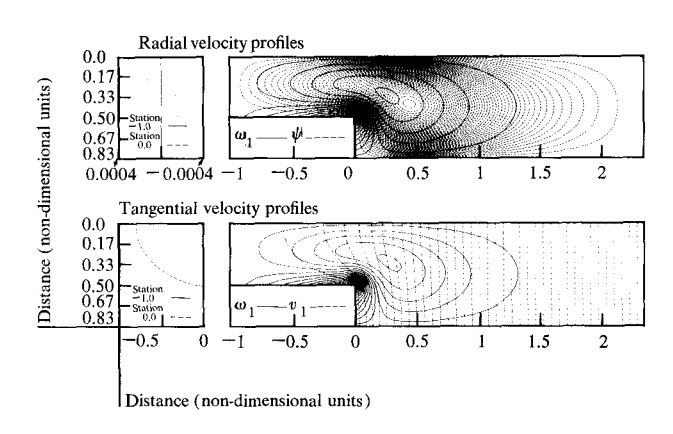


Figure 4 Same as Fig. 3 except  $\varepsilon = 0$ .

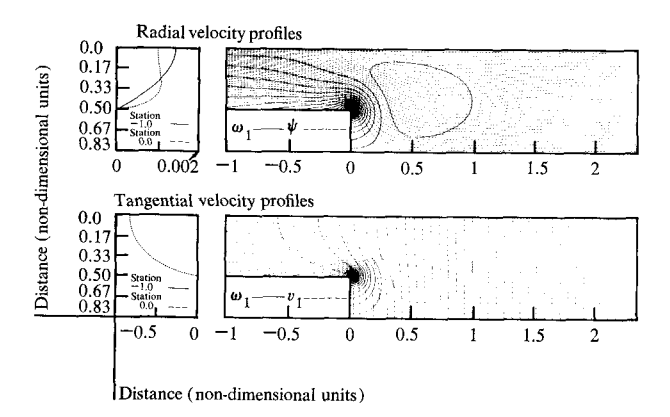


Figure 5 Same as Fig. 3 except  $\varepsilon = 0.00096$ .

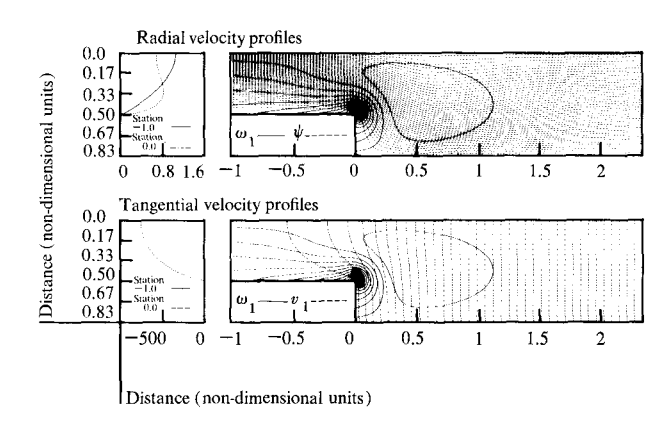


Figure 6 Same as Fig. 3 except  $v_1 = -2000x$  at x = 2.33.

Table 1 Parameter values for exit region flow calculations.

Figure	R=0.133		ω			Ψ			$v_{_1}$			Remarks
	ε	$v_{_{1_x}}$	Min	Мах	Int	Min	Max	Int	Min	Max	Int	
3	0.7	-2.0	-13.2	0.0	1/4	0.0	0.350	1/128	-4.62	0.0	1/8	
4	0.0	-2.0	-0.0188	0.00223	1/2048	-0.0	0.00009	$2 \cdot 10^{-6}$	-4.66	0.0	1/8	
5	0.00096	-2.0	-0.0373	0.00120	1/1024	0.0	0.00048	1/65536	-4.63	0.0	1/8	
6	0.7	-2000.0	-31.3	1.36	1	0.0	0.350	1/128	-4667.0	0.0	128	
17	0.7	-1000.0	-22.1	0.380	1/2	0.0	0.350	1/128	-2333.0	0.0	64	
18	0.7	-1500.0	-26.4	0.792	1/2	0.0	0.350	1/128	-3500.0	0.0	64	~ No shroud test
19	0.5	-1700.0	-24.8	1.22	1/2	0.0	0.250	1/128	-3967.0	0.0	128	
20	0.45	-1000.0	-17.4	0.555	1/2	0.0	0.225	1/256	-2333.0	0.0	64	$\sim\!150and500$ mil
21	0.35	-1625.0	-21.5	1.35	1/2	0.0	0.175	1/256	-3792.0	0.0	64	
22	0.2	-1000.0	-13.0	0.837	1/4	0.0	0.100	1/512	-2329.0	0.0	64	~50-mil shroud
23	0.2	-200.0	-5.59	0.050	1/8	0.0	0.100	1/512	466.7	0.0	8	
24	0.07	-100.0	-2.24	0.040	1/16	0.0	0.035	1/1024	233.3	0.0	4	
25	0.047	-20.0	-1.06	0.00013	1/32	0.0	0.0234	1/2048	-46.7	0.0	1	
26	0.07	-400.0	-5.02	0.344	1/8	0.0	0.0361	1/1024	-938.0	0.0	16	~15-mil shroud
27	0.15	-1300.0	-14.9	1.24	1/2	0.0	0.0948	1/512	-3033.0	0.0	64	
28	0.007	-2000.0	-19.3	2.33	1/2	-0.00005	0.103	1/512	-4671.0	0.0	128	$\sim$ 3-mil shroud
29*	0.35*	-1625.0*	-1218.0	207.0	32	-0.00105	12.8	1/4	-3792.0	0.0	64	High R

\*R = 1.33.

profiles are shown with the same convention. We observe that the profiles at x = -1 agree with those predicted by (8). Also, the exit values indicated at x = 2.33 agree with those predicted by (10); recall that these values were not forced but resulted from the boundary conditions (11). Next, we observe from the streamline plot that no recirculating "Coriolis" vortex occurs near the disk edge. Note that only boundary layer vorticity due to throughflow is in evidence. The radial velocity profile at the disk edge x = 0 is essentially the same as the entrance profile at x = -1. Thus, we conclude that the Poiseuille-type source flow is much stronger than any tendency for recirculation for  $\varepsilon = 0.7$  and R = 0.133.

In order to get an idea of the strength of a disk edge vortex, we calculated the flow for  $\varepsilon=0$ , *i.e.*, for no central air supply. The solution, illustrated in Fig. 4, clearly indicates the disk edge vortex in the streamline plot as well as an obvious extremum in positive (+) vorticity. The radial profile shows no flow at x=-1 but shows the centrally reversed flow at x=0 associated with the Coriolis vortex. The values of stream function indicated in Table 1 for Fig. 4 can be compared with those for Fig. 3 to get an idea of the relative strength of the source flow to the recirculating flow. One can see that the former is roughly a factor of  $10^3$  stronger than the latter. Note, in the lower left graphs of both Figs. 3 and 4, that the relative azimuthal velocity  $v_1$  is almost zero at x=-1.

Next we determined how strong the source could be and still have the disk edge radial profile affected significantly by the vortex recirculation. Using the same boundary conditions as before, we computed the exit flow for R = 0.133 and  $\varepsilon = 0.00096$ . The results are shown in Fig. 5, where we see that no actual recirculation occurs, but that the incipient effect of the Coriolis vorticity is indicated by the centrally inflected radial profile at x = 0. This slow region is associated with the relatively widely spaced streamlines near x = 0.5, z = 0.

In our next numerical calculation we looked for exit boundary conditions other than those given by (11), which could make the disk edge vortex strong enough to overcome the source flow for the experimentally determined values, i.e., for R=0.133,  $\varepsilon=0.7$ . Figure 6 shows the results when all boundary conditions are the same as before, except at x=2.33, where we replaced  $v_{1_{xx}}=0$  in (11) with  $v_1=-2000x$ . Physically, this boundary condition corresponds to a stationary coaxial cylinder with a small radial clearance. On the other hand, it also represents any other external flow that could produce a strong azimuthal velocity gradient. The result is a strong shear layer at the disk edges, which retards the azimuthal flow between the disks at the edge and thereby strengthens the

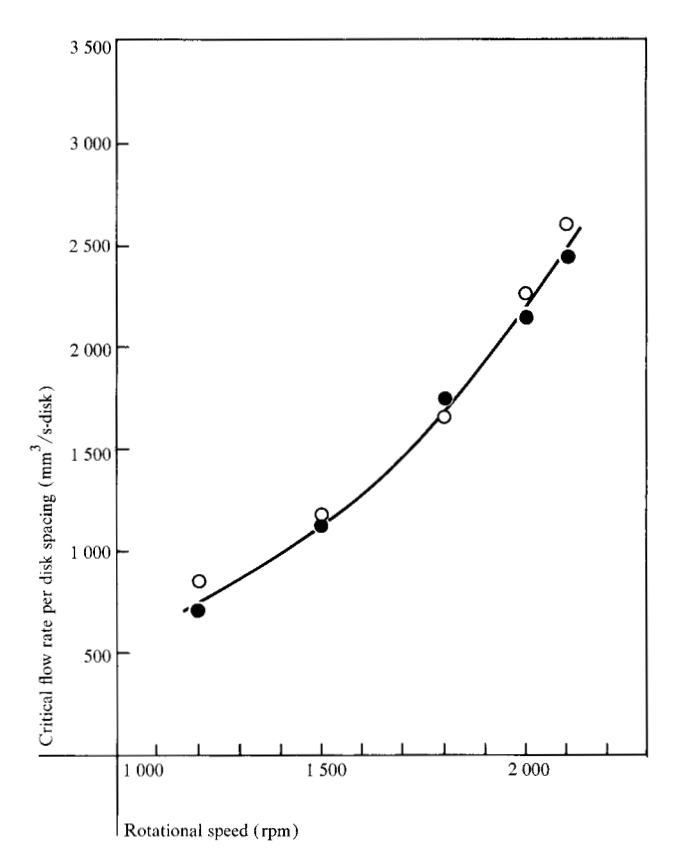


Figure 7 Critical flow  $Q^*$  (per disk) as a function of rotational speed  $\Omega$ .  $\bigcirc$ , s/d = 0.278;  $\bullet$ , s/d = 0.556.

associated vortex. Figure 6 shows these flow features and indicates clearly that the disk edge radial profile is centrally inflected even for the source strength of  $\varepsilon = 0.7$ .

We concluded from these numerical results that the downstream boundary condition is a crucial ingredient in our attempt to describe quantitatively the disk pack instability.

# Experimental study of bistability transition and external flow for shrouded and unshrouded disk packs

We have seen in the previous section that the flow in the exit region between disks depends very much on the downstream boundary conditions. In order to gain a better understanding of the flow just outside the disk pack, we conducted several experiments in which we studied the bistability transition for different disk spacing to disk thickness ratios, s/d, for packs with stationary coaxial shrouds of various radial clearances.

To demonstrate that the bistability transition is due to the air flow and not due to a structural instability, we measured the critical flow rate  $Q^*$  for two different packs,

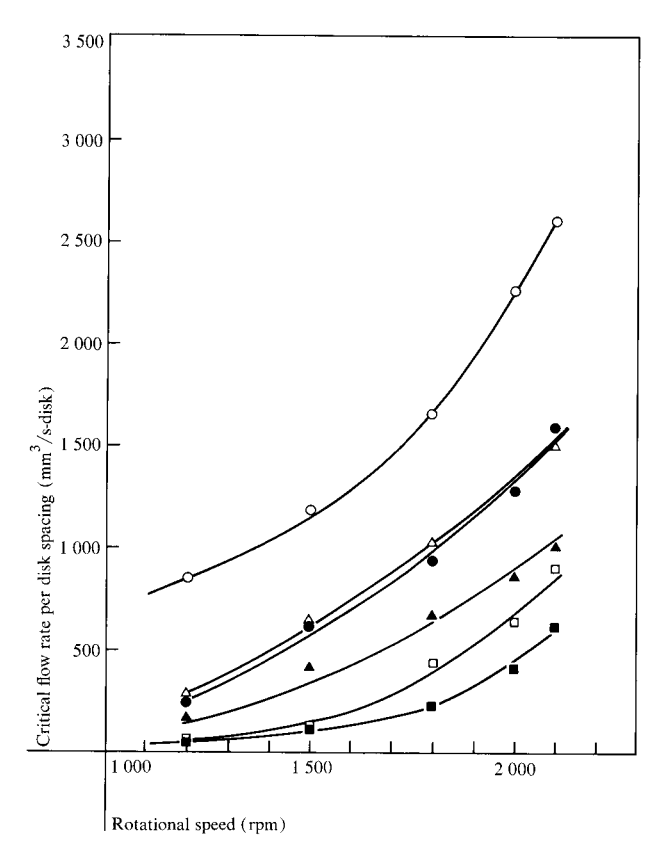


Figure 8 Critical flow  $Q^*$  (per disk) for various shroud clearances as a function of rotational speed  $\Omega$ . Radial shroud clearance:  $\bigcirc$ , no shroud;  $\triangle$ , 500 mil (12.7 mm);  $\bullet$ , 150 mil (3.81 mm);  $\blacktriangle$ , 50 mil (1.27 mm);  $\square$ , 15 mil (0.38 mm);  $\blacksquare$ , 3 mil (0.076 mm).

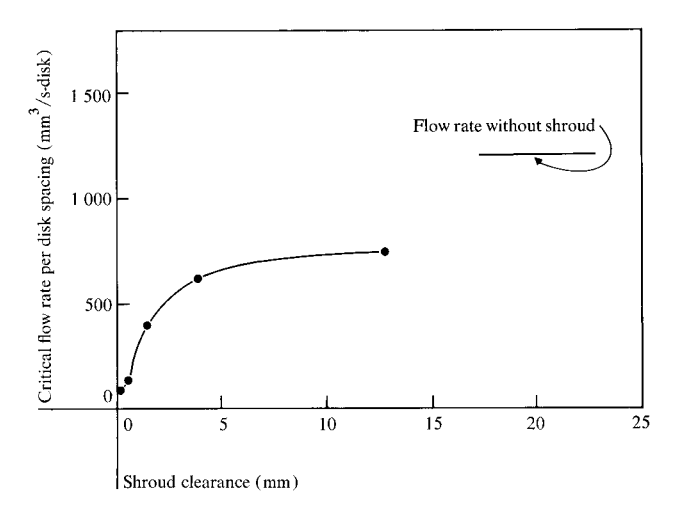


Figure 9 Results of Fig. 8 cross-plotted as a function of clearance at  $\Omega = 1500$  rpm.

one with s/d = 0.278, the other with s/d = 0.556, both having the same spacers. The results are shown in Fig. 7,

where  $Q^*$  is plotted as a function of rotation speed  $\Omega$ . We see that the critical flow rate is essentially the same for the two packs, and thus conclude that the controlling factors are the flow characteristics and not the structural features of the pack.

Next we studied the bistability with different coaxial, stationary, perforated shrouds. We used shrouds with radial clearances of 500, 150, 50, 15, and 3 mil (12.7, 3.81, 1.27, 0.381, and 0.0762 mm). The critical flow rate  $Q^*$ was measured for each as a function of  $\Omega$ . The results are shown in Fig. 8, where we see that the critical flow rate decreases substantially as the radial clearance decreases. Figure 9 shows a cross plot of  $Q^*$  versus shroud spacing at 1500 rpm. The results indicate that less airflow through the disks is required to stabilize the disks as the clearance between the pack and shroud is reduced. Since the shrouds were perforated, ambient pressure was maintained in the annular region between the disk pack and shroud. Thus, the cause for the reduced critical airflow requirement must be related to the effect of the shrouds on the flow field in the annular region. We also observed that no instability was present, even at zero flow rate, for co-rotating shrouds.

The next experiments were an attempt to observe and measure the flow velocities just outside the disk pack. Quantitative measurements are extremely difficult since the variations are superimposed on a much larger azimuthal velocity field. We obtained some qualitative aspects of the flow by use of visual smoke tests and hot wire measurements. The smoke from burned kerosine was introduced into the central air supply and forced through the disk pack. We observed that the velocity field was generally very unsteady, showing bursting of vortices at relatively small distances from the pack. A similar conclusion was also drawn from the hot wire anemometer data. A typical anemometer trace is shown in Fig. 10(a), for which the probe station was 40 mil (1 mm) from the disk edges and centered on a stable, unshrouded pack. The time variations of the modified carrier signal clearly show the unsteady flow field at this location. As the probe is moved away from the disk pack, we observe a decrease in the magnitude of the fluctuations [Figs. 10(a)-(d)]; however, the time-dependent character of the flow is essentially unchanged. When the 500 mil (12.7 mm) clearance stationary shroud was attached, a dramatic decrease in the fluctuation magnitude was observed [Figs. 11(a)-(d)]. Figure 12 shows the results for the unshrouded pack in the unstable, opened condition. Here we see a pulsating, apparently turbulent flow characterized by vortex shedding. The magnitude of these fluctuations is much less dependent on the radial position than was observed for the closed pack condition.

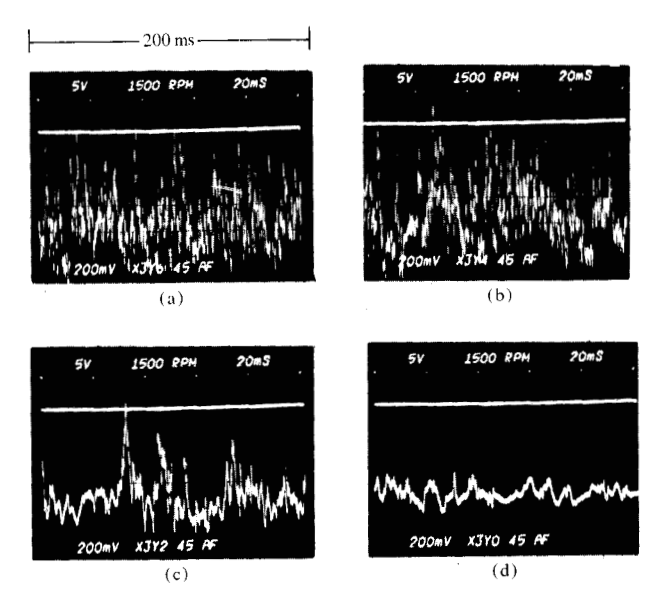


Figure 10 Hot wire probe data for unshrouded disk pack at different radial positions. Distance of hot wire probe tip from pack circumference: (a) 40 mils (1 mm); (b) 150 mils (3.81 mm); (c) 600 mils (15.24 mm); and (d) 1440 mils (36.58 mm).

With these experiments we have established that the presence of a shroud stabilizes the flow field just outside the disk pack and, at the same time, reduces the critical air flow rate. We can conclude that knowledge of this outer flow field is necessary for providing us with realistic downstream boundary conditions for our numerical computations of flow in the exit region.

## Numerical solution of flow between rotating disk pack and stationary shroud

In Ref. [5] we used Eqs. (4)-(7) to obtain the flow field in the annular region formed between the disk edges and a fixed shroud. The radial extent b of this region was assumed to be small compared to the disk radius  $r_0$ . For our calculations, we modeled the disk pack as a cylinder of radius  $r_0$  [which may have outflow given by  $u(r_0) = U$ ]. Figure 13 shows a sketch of the rotating cylinder and fixed coaxial shroud. (It should be noted that the shroud clearance b in this section and in Fig. 13 is unrelated to the exit region dimension b in Fig. 2.) Figure 13 also shows the region of computation in the r, z plane in which the axial extent is usually taken as 2b. The equations given in the second section apply to this problem with slight modification. In all the nondimensionalizations we replace s in (1)–(5) with b. The dimensionless coordinates of the computation region are also shown in Fig. 13.

As a preliminary to these numerical calculations, we first consider the exact axisymmetric steady solution for

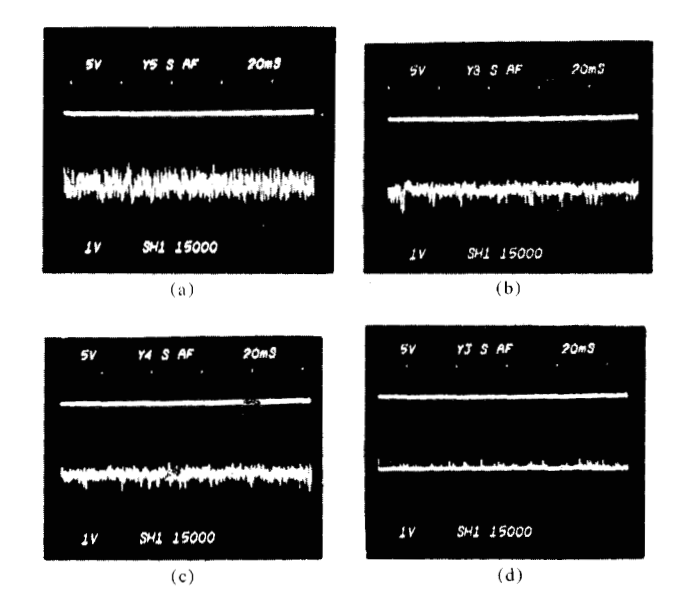


**Figure 11** Hot wire traces for different radial positions for disk pack enclosed by 500 mil (12.7 mm) clearance shroud. Distance of hot wire probe tip from pack circumference: (a) 30 mils (0.762 mm); (b) 140 mils (3.55 mm); (c) 280 mils (7.10 mm); and (d) 500 mils (12.7 mm).

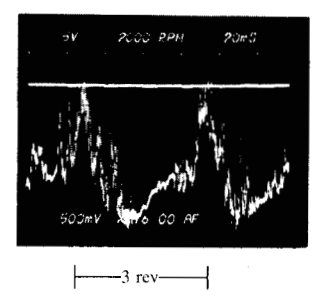


Figure 12 Hot wire trace for unshrouded pack in unstable (opened) mode: probe at 1.44 in. (36.6 mm) from disk edges.

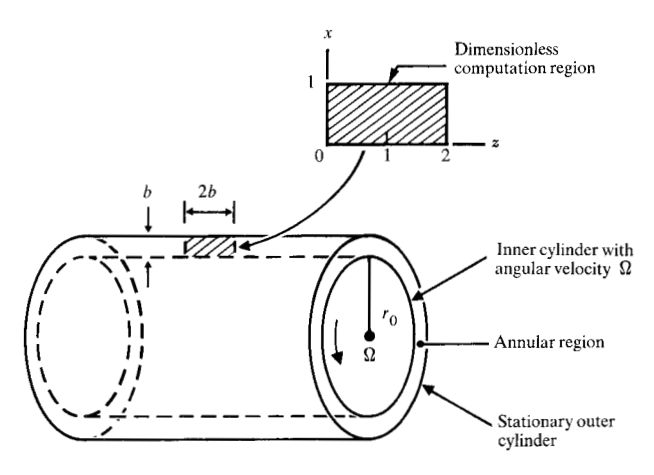


Figure 13 Sketch of coaxial cylinders and computation region.

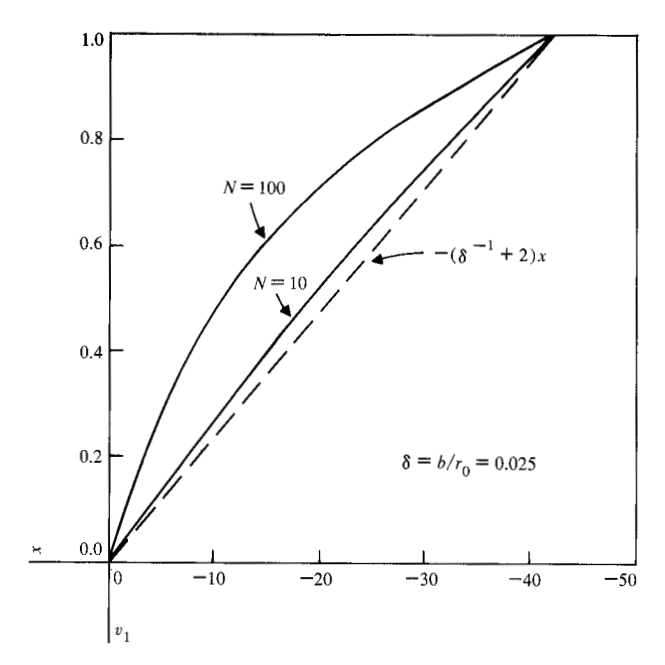


Figure 14 Azimuthal velocity  $v_1$  in circular Couette flow with a central source.

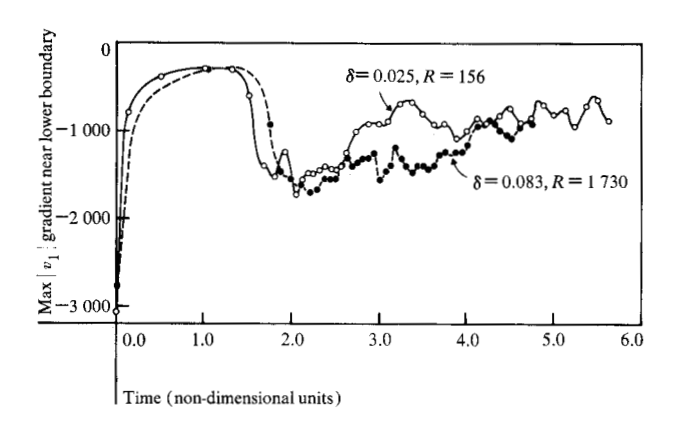


Figure 15 Max  $|v_1|$  at x = 1/200 as a function of t obtained from impulsively started computations for R = 156 and for R = 1730.

laminar Couette flow between porous cylinders with a central supply. Setting  $u=u(r),\ v=v(r),\ w=0,\ u(r_0)=U,\ v(r_0)=r_0\Omega$ , and  $v(r_0+b)=0$ , we obtain the following flow field relative to inertial coordinates (see [2], Section 2):

$$u = Ur_0/r, \qquad \frac{v}{r_0\Omega} = Ar^{N+1} + Br^{-1}$$
 (12)

where

$$A = -\frac{r_0^{-(N+1)}}{(1+\delta)^{N+2} - 1}, \qquad B = \frac{r_0(1+\delta)^{N+2}}{(1+\delta)^{N+2} - 1},$$

$$N = Ur_0/\nu, \qquad \delta = b/r_0. \tag{13}$$

In the perturbation form of the second section, relative to rotating disk coordinates, these results appear as

$$u_1 = U, \qquad v_1 = -\frac{1}{\delta} \left[ \frac{(1+\delta x)^{N+2} - 1}{(1+\delta)^{N+2} - 1} \right] - 2x.$$
 (14)

If  $N\delta = 0(1)$ , no further simplification can be made in (14); but if  $N\delta = 0(\delta)$ , then (14) can be approximated by

$$u_1 = U, \qquad v_1 = -(\delta^{-1} + 2)x.$$
 (15)

This form gives  $v_1$  independent of U and implies that the blowing has no effect on  $v_1$  unless  $N = 0(\delta^{-1})$ .

Figure 14 shows  $v_1 vs. x$  for  $\delta = 0.025$  and for N equals 10 and 100, as computed from (14) and compared with (15). It may be observed from the last section that  $N \approx 75$  for the pack break-up flow rate when the shroud is such that  $\delta = 0.025$ . Note that the gradient of  $v_1$  is reduced near the inner cylinder, and some stabilizing may be expected with blowing if the external flow remains this simple. It will subsequently be shown, however, that the external flow change is more drastic with the onset of instability of this shear layer.

Taylor [3] showed that the laminar circular flow given by (12)-(13) is unstable (for U=0) when certain critical conditions are satisfied. Rosenhead [6], p. 500, gives the critical Taylor number as

$$T_{\rm cr} = (-4A\Omega_0 b^4 / \nu^2)_{\rm cr} = 1,707.8,$$
 (16)

where

$$\Omega_0 = \Omega/2, \qquad A = -\Omega/[(1+\delta)^2 - 1]$$
 (17)

for the case of a fixed outer cylinder and  $\delta << 1$ . This gives

$$T = r_0 b^3 \Omega^2 / \nu^2 = R^2 / \delta, \qquad R = b^2 \Omega / \nu,$$
 (18)

for our configuration. Thus we expect that when the shroud clearance b exceeds a critical value  $b_{\rm cr}$ , Taylor cells will occur at our operating conditions. For all other parameters fixed, (18) gives T proportional to  $b^3$ .

We used an experimental study of Couette instability by Coles [4] to get some indication of what we should expect for our somewhat related configuration. For  $b < b_{\rm cr}$  the solution (12)-(13) is stable, while for  $b > b_{\rm cr}$  various alternatives are expected to occur. There is a small range of b for which the Taylor cells may be "singly periodic," i.e., independent of the azimuthal coordinate. For larger values of b the solution may be "doubly periodic," indicating that the solution is not axisymmetric. As b increases further, the flow is "transitional" and then "turbulent." It should here be emphasized that Coles [4] kept b fixed and varied  $\Omega$  to observe the different regimes. We are interested in corresponding regimes when  $\Omega$  is fixed

and b varies. Also, Cole's results are for small  $r_0$  and hence serve us here only as a qualitative guide.

In Ref. [5] we solved (4)-(7) numerically for the Reynolds number R given by (18), rather than (5), for the region identified in Fig. 13. The boundary conditions used were (15) with U = 0, namely

$$u_1 = 0,$$
  $v_1 = 0,$   $w_1 = 0$  at  $x = 0;$   $u_1 = 0,$   $v_1 = -(\delta^{-1} + 2),$   $w_1 = 0$  at  $x = 1;$  periodicity at  $z = 0, 2.$  (19)

Various initial conditions were employed. These numerical calculations were made primarily for use as downstream boundary conditions in the exit region computations of the second section. The results showed a strong z dependence of the flow field near the inner cylinder. In addition, the solutions were quite unstable for the cases of b = 150 and 500 mil (3.81 and 12.7 mm). The gradient  $v_1$  near x = 0 is the quantity needed for determining our boundary condition, and the maximum and minimum values (over z) of this quantity appear to be fairly stable, as indicated in Fig. 15 even when the general flow field is rapidly changing. We note that the absolute value is at first very large as a result of the strong gradient of the impulsive start initial condition. The gradient rapidly decreases as the strong shear layer diffuses outward. It then begins to increase as the cellular structure starts to form, and remains nearly constant until another cellular structure becomes dominant. On the basis of these results, we see that the steady values of max  $|v_1|$  are about 900 for

 $b=150~{
m mil}$  (3.81 mm) and about 1000 for  $b=500~{
m mil}$  (12.7 mm). The corresponding minimum gradient values were found to be about 100 for all shroud clearances (Fig. 16). The main conclusion to be drawn from the computations heretofore summarized in Figs. 15 and 16, based on calculations in [5], is that the maximum and minimum values of  $|v_{1x}|$  along the inner cylinder are almost independent of the shroud clearance once this clearance exceeds a certain value (about 50 mil in Fig. 16). Thus the values calculated for the widely spaced shroud are applicable to the unshrouded disk pack. We use these values for the exit boundary conditions in the next section.

### Numerical solution for exit region flow—axially varying shear layer downstream condition

In the second section, we showed that a steep azimuthal velocity gradient at the downstream boundary of the exit region could lead to disk edge vortices strong enough to overcome the outward flow and to cause recirculation between the disks near their edges. In the previous section, we showed that the flow outside the rotating disk pack is characterized by values of  $v_{1z}$  near x=0 (i.e., near the

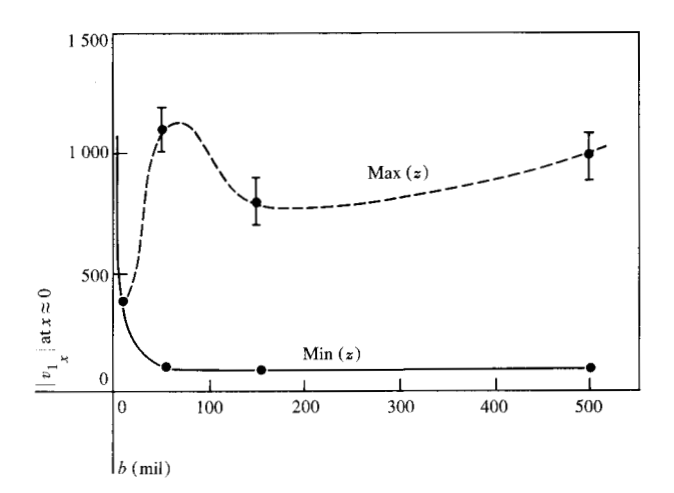


Figure 16 Dependence of max and min  $|v_{1x}|$  at x = 1/200 on dimensionless shroud clearance  $\delta$ .

disk edge), which are of the appropriate magnitude to cause the recirculation. Furthermore, this gradient has a somewhat periodic variation in the axial direction between its maximum and minimum values. For the operating conditions of interest, we obtained the max and min values of  $|v_1|$  at x = 1/200, as shown in Fig. 16. Rather than use these values exclusively as downstream boundary conditions, we performed numerical calculations of the type in the second section for various values of exit velocity  $v_{i}$ and source strength  $\varepsilon$ , all for  $R = s^2 \Omega / \nu = 0.133$ , the value associated with the disk spacing. The basic premise underlying these computations was that the azimuthal velocity gradients at x = 1/200, computed in the last section for a rotating cylinder, determine the downstream boundary value of v, for the closely spaced disk pack. Referring to Fig. 2 and Eq. (11), we replace the boundary condition  $v_{1_{rr}} = 0$  at line 4 of the exit region with

$$v_1 = (v_1)(b/s)$$
 at  $\textcircled{4}$ , (20)

where b here refers to the dimension shown in Fig. 2, and, as in the second section, we chose b/s=7/3 in all the computations. The initial  $v_1$  field was chosen as  $v_1=0$  for x<0 and  $v_1(v_{1_x})x$  for x>0. The results of the exit region flow computations using these boundary conditions are shown in Figs. 17-28. In studying these figures, we can get an idea of the effect of  $\varepsilon$  and  $v_{1_x}$  on the exit region flow field. Figures 17 and 18 show the results for  $\varepsilon=0.7$  and  $v_{1_x}=-1000$  (Fig. 3, the flow for  $v_{1_x}=-2$  shows no disk edge vortex and, furthermore, the radial profiles at  $v_{1_x}=-1000$  (Fig. 3) and  $v_{1_x}=-1000$  (Fig. 17),  $v_{1_x}=-1000$  (Fig. 18), and  $v_{1_x}=-1000$  (Fig. 18), and  $v_{1_x}=-1000$  (Fig. 19) show an influence of

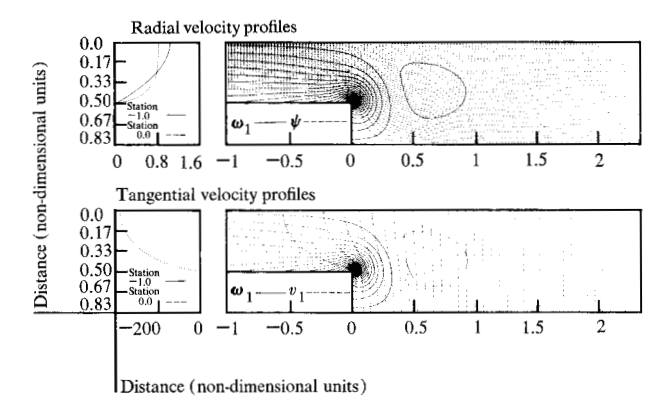
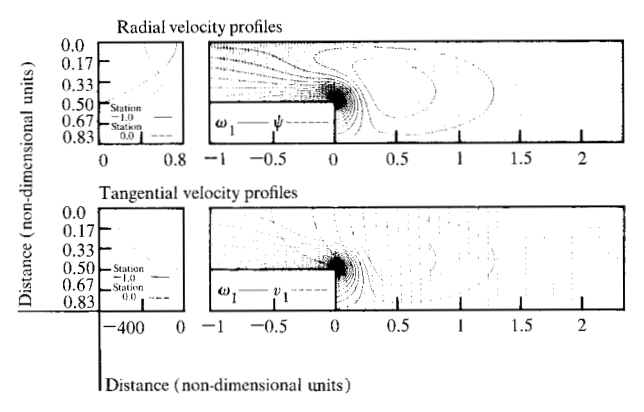


Figure 17 Exit region flow for R = 0.133,  $\varepsilon = 0.7$ ,  $v_{1_x} = -1000$ , t = 0.09.



**Figure 19** Same as Fig. 17 except  $\varepsilon = 0.5$ ,  $v_{1_x} = -1700$ , t = 0.0625.

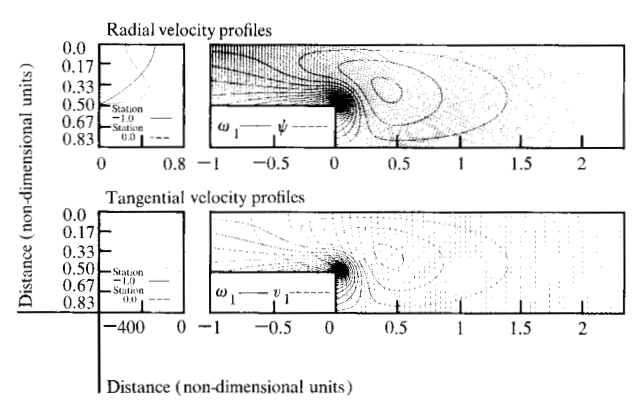
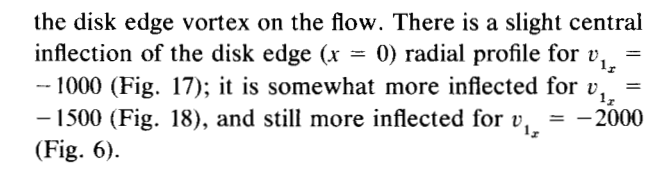
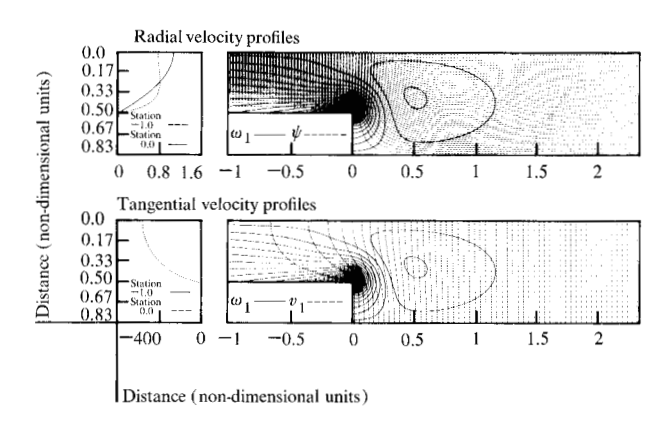
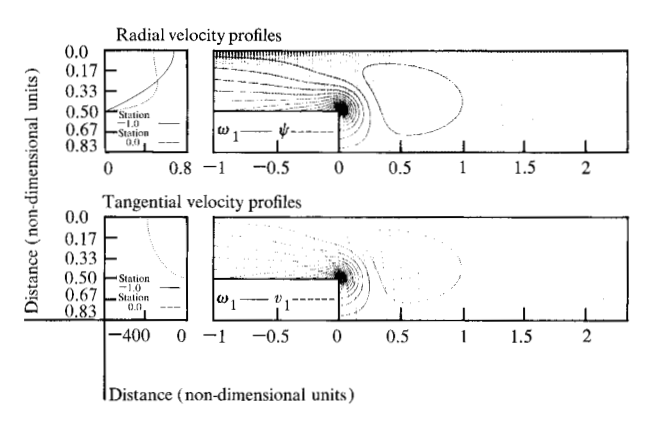


Figure 21 Same as Fig. 17 except  $\varepsilon = 0.35, \, v_{1_x} = -1625, \, t = 0.0625.$ 





**Figure 18** Same as Fig. 17 except  $v_{1x} = -1500$ , t = 0.0625.



**Figure 20** Same as Fig. 17 except  $\varepsilon = 0.45, v_{1x} = -1000, t = 0.0625$ .

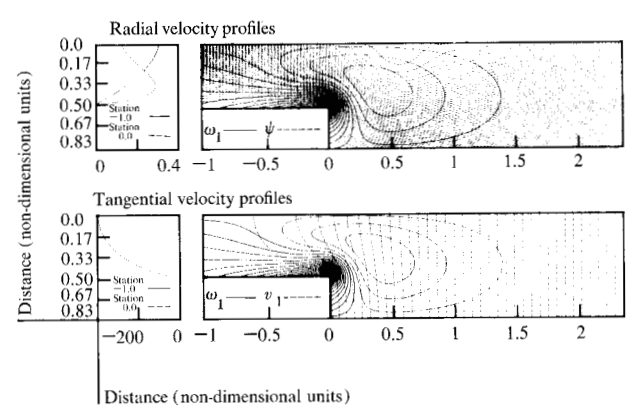


**Figure 22** Same as Fig. 17 except  $\varepsilon = 0.2$ ,  $v_{1x} = -1000$ , t = 0.0625.

Figure 19 shows the flow field for the weaker source  $\varepsilon = 0.5$  with  $v_{1_x} = -1700$ . The disk edge vortex effect is stronger than for the  $\varepsilon = 0.7$  results just discussed. The radial disk edge profile (x = 0) is more inflected at the center. Figure 20 gives results for  $\varepsilon = 0.45$ ,  $v_{1_x} = -1000$ .

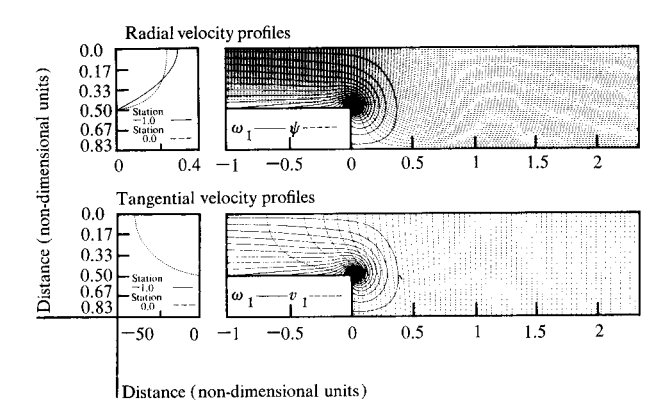


Figure 23 Same as Fig. 17 except  $\varepsilon = 0.2, v_{1x} = -200, t = 0.0625$ .

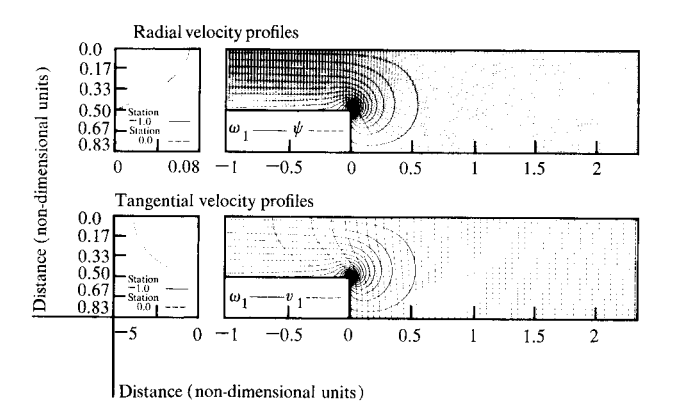


Figure 25 Same as Fig. 17 except  $\varepsilon = 0.047, \ v_{1_x} = -20, \ t = 0.046.$ 

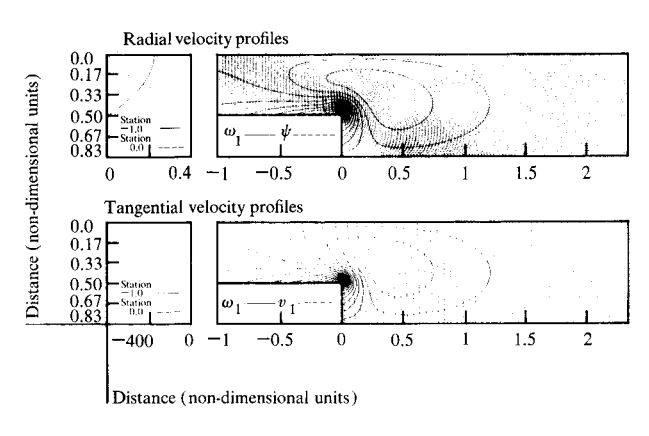


Figure 27 Same as Fig. 17 except  $\varepsilon = 0.15, \, v_{1x} = -1300, \, t = 0.0625.$ 

These results are similar to those in Fig. 18 for  $\varepsilon=0.7$ ,  $v_{1_x}=-1500$ . Figure 21 has parameters  $\varepsilon=0.35$ ,  $v_{1_x}=-1625$ . The central inflection is more pronounced than in Fig. 20. Similar results are obtained in Fig. 22 for  $\varepsilon=0.2$ ,  $v_{1_x}=-1000$ .

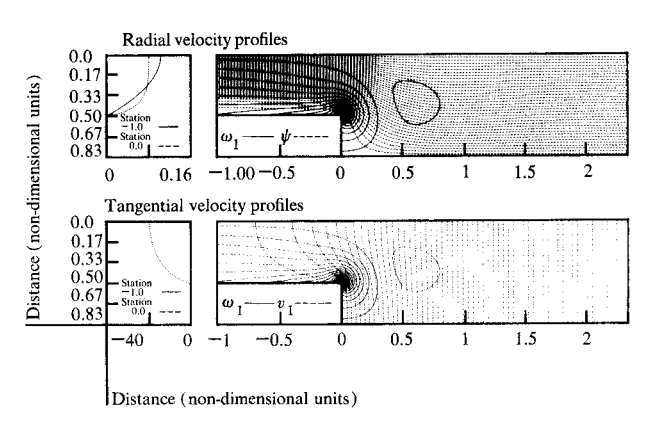
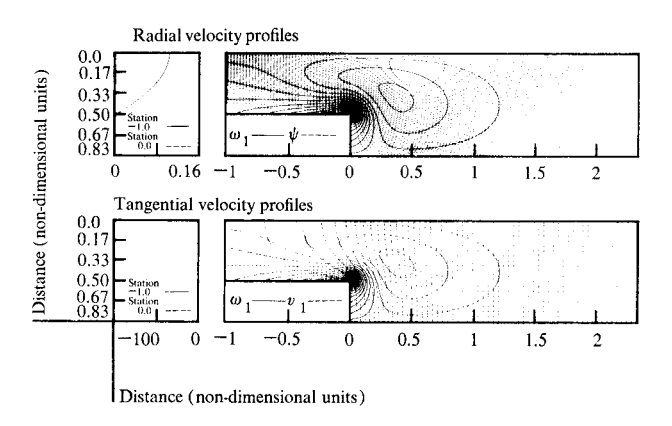


Figure 24 Same as Fig. 17 except  $\varepsilon = 0.07, v_{1x} = -100, t = 0.0625$ .



**Figure 26** Same as Fig. 17 except  $\varepsilon = 0.07$ ,  $v_{1x} = -400$ , t = 0.0625.

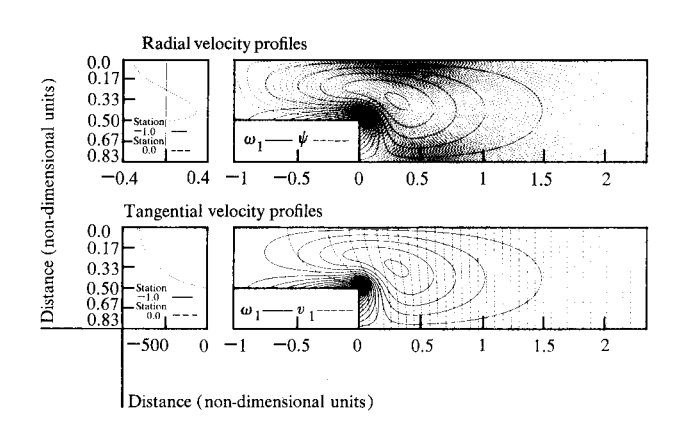
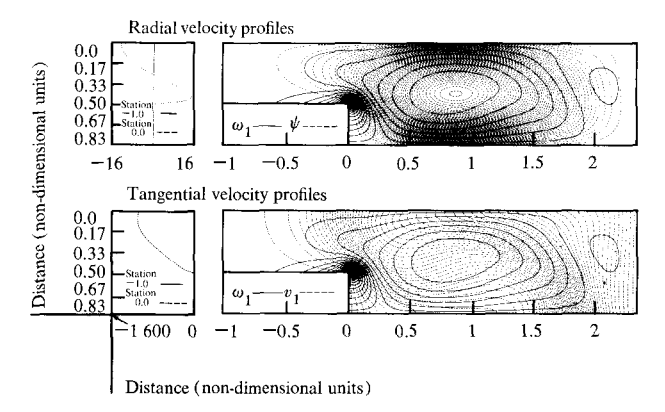


Figure 28 Same as Fig. 17 except  $\varepsilon = 0.007$ ,  $v_{1x} = -2000$ , t = 0.0625.

When  $\varepsilon=0.2$ ,  $v_{1_x}=-200$  (Fig. 23),  $\varepsilon=0.7$ ,  $v_{1_x}=-100$  (Fig. 24), and  $\varepsilon=0.047$ ,  $v_{1_x}=-20$  (Fig. 25), the results are similar to those in Fig. 17. When  $\varepsilon=0.07$  and  $v_{1_x}=-400$  (Fig. 26), the central inflection at x=0 is quite pronounced, but when  $\varepsilon=0.15$  and  $v_{1_x}=-1300$  (Fig. 27),



**Figure 29** Same as Fig. 21 except R = 1.33, t = 0.25.

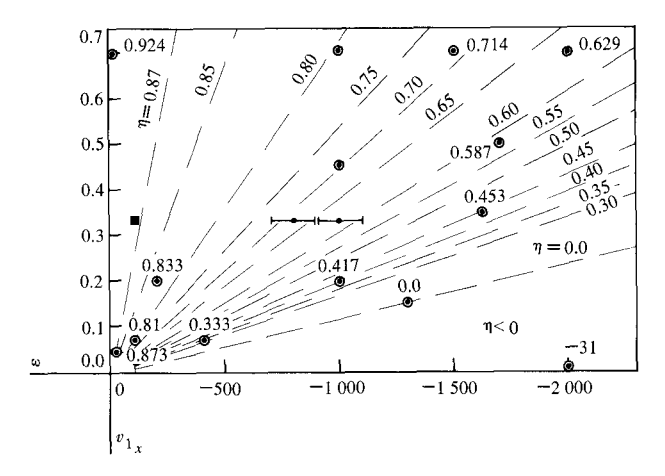


Figure 30 Lines of constant ratio  $\eta = u_1(0, 0)/u_1(0, -1)$  in the  $\varepsilon$ - $v_1$ , plane for R = 0.133, s/d = 1.5.

the disk edge radial profile shows the onset of central backflow. In Fig. 28,  $\varepsilon = 0.007$ ,  $v_{1_x} = -2000$  and we see strong central backflow as in Fig. 4 for  $\varepsilon = 0$ .

Figure 29 with R=1.33 is included to show the effect of increasing R by a factor of 10 from the results in Fig. 21. The results in Fig. 21 were also computed with Fig. 29 as the initial condition to confirm that the same solution would be obtained from different initial conditions. The Fig. 29 result as well as those in [2] indicates that stronger backflow is associated with larger values of R (which increases with spacing s), suggesting, of course, that once an opening is initiated it promotes a further tendency to open.

### Comparison of numerical solution with experimental observations

The numerical results described in the previous section indicate that similar flow fields in the exit region can be associated with the solutions for different sets of values of  $\varepsilon$  and  $v_{1_x}$ . We can take as a measure of the effect of the disk edge vortex on the exit region flow the ratio  $\eta$  defined by

$$\eta = u_1(0, 0)/u_1(0, -1). \tag{21}$$

Figure 30 was prepared from Figs. 3, 6, 17-29. The ratio  $\eta$ heretofore described was computed from each of these figures and recorded at the proper point on the  $\varepsilon$  vs.  $v_1$ graph in Fig. 30. Interpolation between these points allows us to determine straight lines of constant ratio  $\eta$ . All the lines must go through the origin and all the data calculated fit into the straight ray interpolation, as shown. (The reason why these lines should be straight is not apparent.) We observe that this particular graph represents the results only for R = 0.133 and with a disk gap to thickness ratio s/d = 1.5. We see that  $\eta < 1$  (about 0.925) everywhere along the vertical axis, and that  $\eta$  is zero along the ray that goes through  $\varepsilon = 0.15$ ,  $v_{1z} = -1300$  (Fig. 27). All lines of negative ratio represent some central backflow in the disk edge profile. The ratio  $\eta = -\infty$  is along the horizontal axis;  $\eta = -31$  occurs on the ray that passes through  $\varepsilon = 0.007$ ,  $v_{1} = -2000$  (Fig. 28). When the ratio is about 0.8 (Fig. 17), the disk edge profile appears weakly inflected by the edge vortices. When the ratio is less than 0.5 (Fig. 21), the disk edge profile appears strongly inflected.

The two solid circles with bars in Fig. 30 show the approximate measured critical flow rate (~0.35), for fixed shrouds (Fig. 9), plotted against the maximum steady  $v_1$ as computed in the last section and plotted in Fig. 16 for b = 150 and 500. The solid square in Fig. 30 shows the same flow rate plotted against the corresponding (and common) minimum steady  $v_1$ . The qualitative appearance of flow fields and profiles expected with these values of  $\varepsilon$ ,  $v_1$  can be deduced by looking at the figures corresponding to the  $\varepsilon$ ,  $v_1$  pairs which produced, through numerical computation, the ratio  $\eta$  closest to the ratio ray that passes through the points of interest. Thus, Fig. 6  $(\eta = 0.629)$  and Fig. 20  $(\eta = 0.70)$  correspond to the maximum gradient for b = 150 and 500 mil (3.81 and 12.7 mm), while the minimum gradient would look somewhat like Fig. 25 ( $\eta = 0.873$ ). The max gradient fields have the ratio  $\eta \simeq 0.65$  and the min gradient fields have  $\eta \simeq 0.90$  for  $\varepsilon \simeq$ 0.35.

### Conclusions

Experimental investigations have shown that the disk pack transition from the bistable to unstable regime which occurs when the air flow rate is decreased to  $Q^*$  is due to the flow characteristics at the disk edges.

Numerical calculations for the flow in the outer region of the pack have confirmed that backflow into the disks

can be controlled by the outflow rate. The required rate depends strongly on the external flow conditions.

Calculation of the external flow for various shroud spacings reveals that the outer flow field exhibits strong axial variations. These variations are of sufficient magnitude to account for the pack breakup in accordance with the exit region recirculation hypothesis. For wide shroud spacing the azimuthal velocity tends to form an unstable boundary layer at the disk edges that locally shoots out azimuthal vorticity. At these locations the boundary layer temporarily loses its strength and thereby causes strong axial variations.

The axial variation in the boundary layer gives a corresponding axial variation in the downstream boundary condition for the pack flow. Since the outflow rate remains the same for all disks, this causes an axial periodicity in the disk edge flow recirculation. The recirculation is strongest where the external shear layer is strongest (highest magnitude of  $v_{1x}$ ). The pressure between the disks is also highest where the external boundary layer is strongest. Disk spacing tends to increase in the high pressure regions and decrease in the low pressure ones, and the recirculation becomes stronger at the wider spaced disks and weaker at the closer ones. Thus, the pack break-up mechanism is self-strengthening, and the result is a collapse into the subpack-gap configuration.

The numerical results are in excellent quantitative agreement with the experimental observations. They predict not only the correct order of magnitude for the critical flow rate but also the axial periodicity of the instability. Predictions for a wide range of physical parameters are possible using the discussed two-stage model.

#### References

- 1. B. W. McGinnis, A. W. Orlando, and J. A. Weidenhammer, "Bistable Deflection Separation of Flexible Disks," U.S. Patent #3,936,880, February 1976.
- 2. D. B. Bogy, J. E. Fromm, and F. E. Talke, "Exit Region Central Source Flow Between Finite Closely Spaced Parallel Co-rotating Disks," *Phys. Fluids* 20, 176-186 (1977).
- 3. G. I. Taylor, "Stability of a Viscous Liquid Contained Between Two Rotating Cylinders," *Phil. Trans. Roy. Soc. A* 223, 289-343 (1923).
- 4. D. Coles, "Transition in Circular Couette Flow," J. Fluid Mech. 21, 385-425 (1965).
- D. B. Bogy, J. E. Fromm, and F. E. Talke, "Flow Near an Impulsively Rotated Cylinder," to be published.
- Laminar Boundary Layers, L. Rosenhead, ed., in Fluid Motion Memoirs, Oxford University Press, London, 1963.

Received October 19, 1978; revised December 22, 1978

D. B. Bogy is located at the University of California, Berkeley, California 94720; J. E. Fromm and F. E. Talke are located at the IBM Research Division laboratory, 5600 Cottle Road, San Jose, California 95193.